Novel insights from Fe-isotopes into the lithological heterogeneity of Ocean Island Basalts and plume-influenced MORBs

Matthew L.M. Gleeson [*], Sally A. Gibson, Helen M. Williams

Department of Earth Sciences, University of Cambridge, Downing Street, Cambridge, CB2 3EQ, UK

ARTICLE INFO

ABSTRACT

The extent of lithological heterogeneity in the Earth's convecting mantle is highly debated. Whilst the presence of pyroxenite in the mantle source regions of Ocean Island Basalts (OIBs) has traditionally been constrained using the minor-element chemistry of olivine phenocrysts, recent studies have shown that the Ni and Mn contents of primitive olivines are influenced by the conditions of mantle melting, as well as magma chamber processes. Nevertheless, constraining the lithological properties of the mantle is important due to its influence on the P-T path followed by solid mantle material during adiabatic ascent, as well as the density of upwelling mantle plumes. We have therefore explored the use of Fe-isotopes as a novel method of tracing lithological heterogeneity in the mantle source regions beneath plume-influenced segments of the global Mid-Ocean Ridge system as well as OIBs.

We present new Fe-isotope (δ^{56}Fe) and trace-element data for 26 basaltic glasses from the plume-influenced Galápagos Spreading Centre to investigate the relative roles of pyroxenite and peridotite in the mantle source region of oceanic basalts. Our data reveals significant heterogeneity in the Fe-isotope composition of the Galápagos Spreading Centre basalts ($+0.05$ to $+0.25$‰ δ^{56}Fe), which correlates with key major- and trace-element parameters (e.g. $CaO_{(8)}/Al_2O_{3(8)}$, $[La/Sm]_n$). Application of new models developed to calculate Fe-isotope fractionation during mantle melting, alongside Monte Carlo simulations for melting of a 2-component peridotite mantle, show that this variation cannot be caused by changes in melting processes and/or oxygen fugacity of a peridotitic mantle. Instead, our new δ^{56}Fe data is best explained by variations in the proportion of isotopically-heavy pyroxenite-derived melt that contributes to the GSC basalts, and conclusively shows that lithological heterogeneity exists in the Galápagos mantle plume. Our findings have implications for the moderately-heavy δ^{56}Fe compositions measured in plume-influenced basalts from the Society Islands, Rochambeau Ridges of the Lau back-arc basin, and the FAMOUS segment of the Mid-Atlantic Ridge, which we suggest may also represent contribution from pyroxenite-derived melts.

© 2020 Elsevier B.V. All rights reserved.

1. Introduction

Seismic tomography and distinctive geochemical signatures of Ocean Island Basalts (OIBs) and Mid-Ocean Ridge Basalts (MORBs) provide compelling evidence for recycling of lithospheric components into the convecting mantle, and subsequent incorporation of this material into upwelling mantle plumes (Hofmann, 1997; van der Hilst et al., 1997). Whilst the presence of recycled material in the Earth's mantle, and its lithological properties (i.e. relative modal proportions of olivine and pyroxene), have important implications for mantle dynamics and the density of upwelling mantle

plumes (Shorttle et al., 2014), the nature and abundance of these components is poorly constrained.

Incorporation of recycled oceanic lithosphere into the convecting mantle is widely believed to result in the presence of lithologically-distinct components via high-pressure melting of eclogite (metamorphosed remnants of recycled slabs), and subsequent reaction of these melts with surrounding peridotite (Sobolev et al., 2007). This results in the formation of pyroxene-rich (and highly fusible) components in the mantle (pyroxenite; Sobolev et al., 2007; Yaxley and Green, 1998). Identification of this lithologically-distinct material in the mantle source region of OIBs and MORBs has classically been achieved using minor-element concentrations in olivine (Herzberg, 2011; Sobolev et al., 2007), major-element compositions of high MgO basalts (Lambart et al., 2013), and ratios of first row transition elements (Davis et al., 2013). However, these methods are subject to considerable

uncertainties regarding: (i) the influence of temperature, pressure, and oxygen fugacity (fO_2) during mantle melting (Matzen et al., 2017b); and (ii) the influence that crustal processes may play (Gleeson and Gibson, 2019). In particular, it is still uncertain whether Ca, Ni, and Mn concentrations in magmatic olivines can be used, unambiguously, to distinguish between peridotite and pyroxenite derived melts and it is therefore important to develop additional tracers for pyroxenite melting (Gleeson and Gibson, 2019; Matzen et al., 2017b; 2017a; Putirka et al., 2011; Rhodes et al., 2012).

Here we investigate the use of stable Fe-isotopes ($\delta^{56}Fe$) as an alternative method for identifying lithological heterogeneity in the mantle source region of oceanic basalts (Konter et al., 2016; Nebel et al., 2019; Williams and Bizimis, 2014). As Fe is stoichiometrically incorporated into mantle minerals, variations in $\delta^{56}Fe$ likely represent changes in the mass fraction contribution from different mantle components. Therefore, variations in $\delta^{56}Fe$ have the potential to provide a very different perspective on mantle heterogeneity compared to traditional radiogenic isotope ratios (e.g. Sr, Pb) that tend to be dominated by relatively small contributions from enriched mantle components and yield little information on mantle lithology.

Traditional stable isotope theory predicts that the extent of isotopic fractionation (i.e. $\Delta^{56}Fe_{A-B} = \delta^{56}Fe_A - \delta^{56}Fe_B$; where $\delta^{56}Fe$ represents the deviation in $^{56}Fe/^{54}Fe$ from the IRMM-014 standard in parts-per-thousand) is inversely proportional to temperature (i.e. $1/T^2$). Despite the high temperature of igneous processes, recent advances have revealed that magmatic processes (e.g. mantle melting/crystal fractionation) can cause both kinetic and equilibrium stable-isotope fractionation in these systems (Dauphas et al., 2014; Huang et al., 2010; Schuessler et al., 2009; Sossi and O'Neill, 2017; Teng et al., 2011, 2008; Weyer and Ionov, 2007; Zhao et al., 2017). In particular, Fe-isotopes possess relatively large and predictable equilibrium fractionation factors between different minerals and/or melts at magmatic temperatures, due to the polyvalent nature of Fe, as well as variations in the coordination state of Fe in different mineral phases (Sossi and O'Neill, 2017). As heavy Fe-isotopes (e.g. ^{56}Fe, ^{57}Fe) should be preferentially partitioned into the phase with the strongest Fe-O bonds, minerals that incorporate small amounts of Fe^{3+} (e.g. pyroxene) are predicted to have heavier $\delta^{56}Fe$ compositions than those that are deficient in Fe^{3+} (e.g. olivine; Sossi and O'Neill, 2017). This is because the smaller ionic radii and higher valence state of Fe^{3+} results in shorter, and hence stronger, Fe-O bonds (Dauphas et al., 2014).

Due to the non-modal nature of melting in the convecting mantle (i.e. disproportionately high contribution from isotopically-heavy clinopyroxene to the melt phase), and the incompatible nature of Fe^{3+}, primary mantle melts are predicted to be isotopically heavy compared to their mantle source (Dauphas et al., 2009; Williams and Bizimis, 2014). The extent of the Fe-isotope fractionation is also believed to be sensitive to the fO_2 of the mantle, which has previously been used to explain the offset between the average $\delta^{56}Fe$ composition of the terrestrial mantle ($\delta^{56}Fe = +0.025 \pm 0.025$‰; based on analyses of abyssal peridotites; Craddock et al., 2013) and MORBs ($\delta^{56}Fe \sim +0.1$‰; Sossi et al., 2016; Teng et al., 2013). Alternatively, some studies have suggested that the extent of isotopic fractionation during mantle melting may be sensitive to the lithological properties of the source (Sossi and O'Neill, 2017; Williams and Bizimis, 2014). This is due to the greater isotopic fractionation during melting of pyroxene-rich mantle rather than peridotite (Williams and Bizimis, 2014), and the heavy $\delta^{56}Fe$ of pyroxenitic components regardless of formation mechanism (Konter et al., 2016; Nebel et al., 2019; Williams and Bizimis, 2014).

Our study is primarily focused on the Fe-isotope composition of basalts erupted at regularly-spaced intervals on segments of
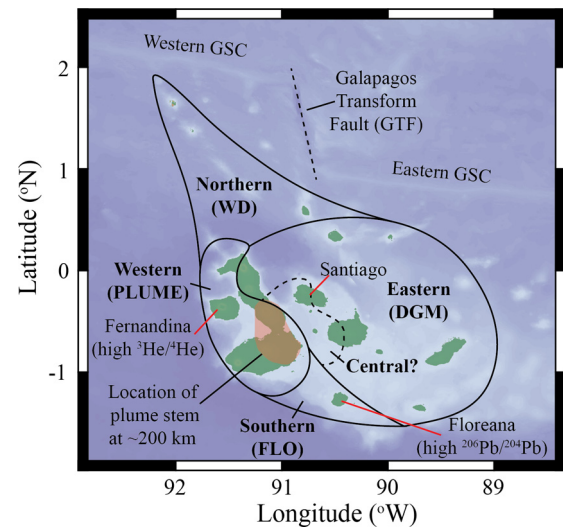

Fig. 1. Map of the Galápagos Archipelago highlighting the geographic distribution of the 4 isotopic components that have been previously identified on the basis of Sr, Nd, Pb and He isotopes (adapted from Hoernle et al., 2000). These components correspond to the FLO, DGM, WD, and PLUME components identified by Harpp and White (2001). We have also included a region which we term the central isotopic component. This represents the region of the Galápagos Archipelago where a pyroxenitic signature is apparent in the major-element chemistry of mildly-alkaline basalts that are isotopically similar to the enriched mantle component identified beneath the Galápagos Spreading Centre (Appendix A; see Section 7). The location of the mantle plume at 200 km depth is from the seismic tomography study of Villagómez et al. (2014). (For interpretation of the colours in the figure, the reader is referred to the web version of this article.)

the Galápagos Spreading Centre (GSC) that are influenced by the nearby Galápagos mantle plume (Schilling et al., 2003). These samples exhibit considerable variability in their incompatible trace-element compositions and Sr, Nd and Pb isotope ratios, and range from compositions more depleted than average MORBs to highly enriched basalts (Gibson and Richards, 2018; Schilling et al., 2003). If lithological heterogeneity exists in the mantle source region beneath the GSC then it is highly likely to be expressed in the $\delta^{56}Fe$ composition of these samples.

2. Geological background

The Galápagos Archipelago (eastern equatorial Pacific) represents one of the most volcanically active regions in the world. The broad geographic distribution of Holocene volcanism in the Galápagos has allowed multiple geochemical studies to place constraints on the spatial heterogeneity of radiogenic isotope ratios in the Galápagos mantle plume (Harpp and White, 2001; White et al., 1993). Analyses of basaltic lavas from across the Galápagos Archipelago reveal the presence of at least 3 isotopically-enriched mantle components that form a horseshoe shape around an isotopically-depleted eastern component (DGM; Fig. 1; Harpp and White, 2001; Hoernle et al., 2000; White et al., 1993).

The 'Western' (PLUME) Galápagos plume component is characterised by high $^3He/^4He$ ratios and moderately radiogenic Sr and Pb-isotope values (similar to the common plume component referred to as 'FOZO' or 'C'; Hart et al., 1992) and is believed to contain a significant contribution from the primordial mantle (Kurz and Geist, 1999). The 'Southern' (FLO) component is characterised by the most radiogenic Sr and Pb-isotope ratios in the Galápagos. The Pb-isotope signature of the FLO plume component is similar to the global HIMU end-member, although the presence of an EM-type component is required to explain the $^{87}Sr/^{86}Sr$ signatures from this region (Harpp et al., 2014). Recent studies have suggested that this component may represent recycled oceanic crust (Harpp et al., 2014), although olivine chemistry is inconsistent with the
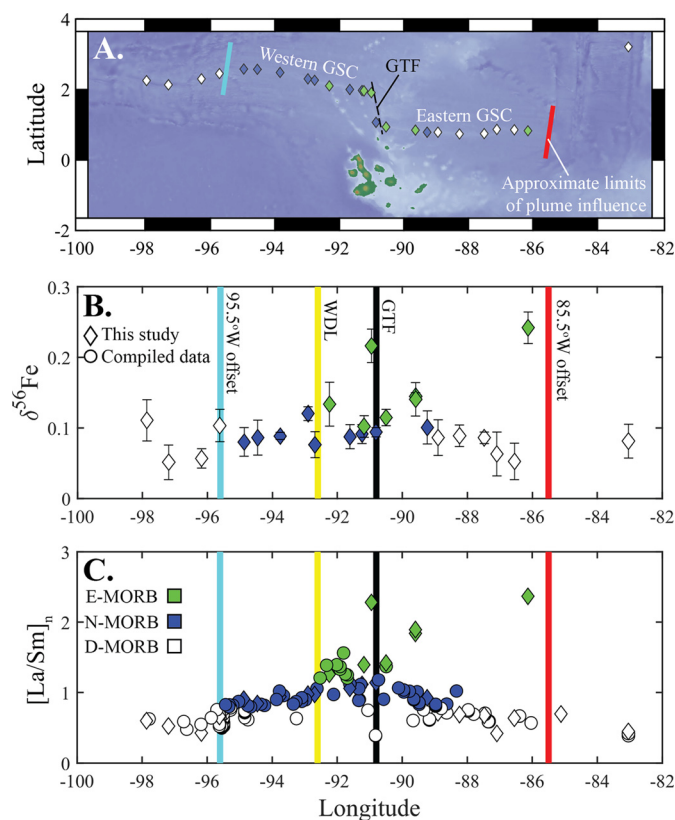
Fig. 2. Longitudinal variation in key geochemical parameters on the GSC. Panel **A.** shows the location of the samples analysed in this study and the region of the Galápagos Spreading Centre that is believed to be influenced by the Galápagos mantle plume (the approximate limits of plume influence are shown by the blue and red lines; Gibson and Richards, 2018). Panel **B.** shows the range of δ^{56}Fe compositions measured in the GSC basalts. Panel **C.** shows the variation in the $[La/Sm]_n$ ratio of the GSC basalts, which is used to define 3 geochemical groups. In this study E-MORBs are defined as any basalt with a $[La/Sm]_n$ ratio greater than 1.2, D-MORBs are defined as any basalt where the $[La/Sm]_n$ ratio is less than 0.8 (where the n represents normalisation to the primitive mantle value of Sun and McDonough (1989)). GTF and WDL correspond to the Galapagos Transform Fault and Wolf-Darwin Lineament respectively. (For interpretation of the colours in the figure, the reader is referred to the web version of this article.)

presence of a lithologically-distinct pyroxenite (Vidito et al., 2013). The 'Northern' (Wolf-Darwin; WD) Galápagos plume component is characterised by elevated ^{208}Pb/^{206}Pb and ^{207}Pb/^{206}Pb ratios. Less is known about the origin of this component than the FLO and PLUME components (Harpp and White, 2001).

The isotopic heterogeneity observed in plume-derived basalts from across the Galápagos Archipelago is evident in the composition of basalts (D-, N-, and E-MORBs) erupted along the nearest section of the GSC (Gibson et al., 2015), ∼150–250 km north of the centre of plume upwelling (Fig. 2). The geochemical heterogeneity displayed by these GSC basalts coincide with variations in geophysical parameters along the GSC (e.g. crustal thickness, bouguer gravity anomalies; Ingle et al., 2010; Mittelstaedt et al., 2014; Schilling et al., 2003). These signatures are thought to result from the transfer of compositionally, and thermally, distinct material from the off-axis Galápagos plume.

Several studies have hypothesised that the geochemical variations displayed by the GSC basalts result from incorporation and mixing of melts from three isotopically distinct components (Gibson et al., 2015; Ingle et al., 2010; Schilling et al., 2003). A sharp change in Ba/Nb, ^{3}He/^{4}He and Δ^{208}Pb across the Galápagos Transform Fault (GTF) at 91°W reveals the incorporation of the WD Galápagos plume component in the shallow mantle beneath the western GSC (but not beneath the eastern GSC; Gibson et al.,

2015). In addition, E-MORBs found within ∼200 km of the Galápagos Transform Fault contain a significant contribution from low-fraction melts of an isotopically-enriched component in the Galápagos plume (Gibson and Richards, 2018; Ingle et al., 2010). However, the radiogenic isotope composition of this component is debated with some authors suggesting FOZO or C-like compositions (Ingle et al., 2010), whereas others have suggested that this component is similar to the global HIMU endmember (Gibson et al., 2015; Schilling et al., 2003).

We use our new Fe-isotope data from the GSC to evaluate whether any of previously identified components in the Galápagos mantle plume, defined on the basis of Sr, Nd and Pb isotopic ratios (Hoernle et al., 2000; Harpp and White, 2001), are associated with a lithologically-distinct mantle source. This is achieved by integrating 2-component mantle melting models with theoretical predictions of Fe isotope fractionation to constrain the Pb-isotope composition of the isotopically-enriched pyroxenite component that is common to basalts erupted on both the western and eastern GSC. This allows us to place new constraints on the extent and location of lithological heterogeneity in the Galápagos mantle plume.

3. Samples

Twenty-six basaltic glasses from 83°W–98°W on the Galápagos Spreading Centre (GSC) were selected from the J.G. Schilling collection at the University of Rhode Island and analysed for Fe-isotopes. Most of these samples have a geographical spacing of ∼30–40 km and span the entire range of incompatible trace-element and radiogenic isotope compositions displayed by GSC basalts (Schilling et al., 2003).

To ensure that our Fe-isotope data represents the composition of GSC basaltic melts that are unaffected by alteration or crystal accumulation (McCoy-West et al., 2018), chips of basaltic glass (approximately 5 mm diameter) with no visible signs of alteration/oxidation or notable phenocrysts were hand-picked using a binocular microscope. Backscatter Electron imaging of these samples confirmed that the proportion of olivine and clinopyroxene in each sample was extremely low (<1%).

4. Analytical methods

Prior to Fe-isotope analysis, we analysed the major- and minor-element concentrations of characteristic glass chips from each sample using a Cameca SX100 EPMA in the Department of Earth Sciences at the University of Cambridge. Analysis was carried out using a beam current of 10 nA, an accelerating volatile of 15 kV, and a defocused beam (10 μm). Peak count times of 10 s were used for Na and K (which were analysed first), and 20 s for Ca, Si, Mg, Al, and Fe. Minor elements were analysed for 60 s (P, Ti, Cr and Mn). Background counts were collected either side of the peak for half the peak count times. Data quality was checked using three secondary glass standards (two basaltic – including VG-2, one rhyolitic; see Appendix A). Measured compositions are consistently within 1 standard deviation of the preferred values and a precision of <3% was regularly achieved for all major elements except Na (<4%).

Trace-element concentrations were acquired using a 193ESI Laser Ablation system coupled to a Nexion Perkin Elmer inductively coupled plasma mass spectrometer (ICP-MS) in the Department of Earth Sciences, University of Cambridge. Following systematic testing of laser ablation analysis of volcanic glass over a range of spot sizes, fluence and repetition rates, we selected a spot size of 100 μm, fluence of 8 J/cm^2 and repetition rate of 10 Hz for our analysis. Data was only collected from regions of clean, microlite-free, glass so that our analyses were not influenced by accidental ablation of plagioclase microlites. Data reduction was

performed using Glitter software[©], and then later re-processed in Iolite[©] with no significant difference observed in the calculated values. ^{29}Si was used as an internal standard, and NIST SRM612 as a primary standard. Repeated measurements of BHVO-2g and BIR-1g secondary standards reveal that a precision of $<5\%$ was achieved for most trace elements, and most first-row transition elements (FRTEs). Slightly larger errors (precision of $<10\%$) are seen for the heavy rare earth element (HREE) which are only present in low concentrations. Repeated analyses of secondary standards are regularly within 95% and 105% of published values for all elements reported.

Once appropriate chips of each sample of basaltic glass had been chosen, sample dissolution, iron purification and isotopic analyses were carried out in the Department of Earth Sciences, University of Cambridge. Isotopic analyses were performed on a Thermo Neptune multiple-collector ICP-MS. Sample solutions consisted of $\sim$8.6 ppm Fe in 0.1 M HNO$_3$. Instrumental mass bias was corrected for by sample standard bracketing, where the sample and standard Fe beam intensities were matched to within 10%. Mass dependence and reproducibility were evaluated using an in-house 'iron chloride' salt standard (δ^{56}Fe $= -0.70 \pm 0.05\%$; δ^{57}Fe $= -1.08 \pm 0.07\%$) that has been analysed in previous studies (Williams and Bizimis, 2014). Chemistry blanks possessed negligible amounts of Fe compared to our samples (<5 ng). The analytical precision of our Fe-isotope analyses is based on between 6 and 12 repeat measurements for each sample and is generally found to be better than $\pm 0.025\%$ (2σ for δ^{56}Fe; Table 1). The accuracy of the Fe-isotope analysis was monitored using the USGS BIR-1 secondary standard (δ^{56}Fe $= +0.056 \pm 0.031\%$ (2σ); δ^{57}Fe $= +0.081 \pm 0.048\%$ (2σ); n $= 9$) and was found to be consistent with previous studies (Dauphas et al., 2009; Williams and Bizimis, 2014).

5. Results

We use primitive mantle normalised [La/Sm]$_n$ ratios to define three geochemical types of basalts: E-MORBs ([La/Sm]$_n > 1.2$); N-MORBs ($0.8 <$ [La/Sm]$_n < 1.2$); and D-MORBs ([La/Sm]$_n < 0.8$). The N-MORB–E-MORB transition is lower than that suggested by Gale et al. (2014) due to the overall depleted nature of basalts from the Galápagos Spreading Centre. E-MORBs are generally found in the region of greatest plume-influence (between 89.5°W and 92.6°W; Christie et al., 2005; Cushman et al., 2004; Detrick et al., 2002; Gibson et al., 2015; Ingle et al., 2010). In addition, several of the samples that have been analysed from the GSC possess anomalously enriched trace-element compositions ([Sm/Yb]$_n > 1.5$). This is believed to represent short-length scale heterogeneity in the delivery of enriched material to the GSC (Gibson and Richards, 2018).

Clear differences are also seen in the major-element systematics of D-MORBs, N-MORBs, and E-MORBs from the GSC. These relate to variations in the depth of mantle melting (e.g. lower SiO$_2$ in E-MORBs; Lee et al., 2009) as well as variations in the source properties and/or initial water content of these magmas (e.g. lower FeO$_t$ and CaO/Al$_2$O$_3$ in E-MORBs; Appendix A). These differences indicate that E-MORBs contain greater contributions of high-pressure (i.e. garnet stability field), H$_2$O-rich mantle melts (Gibson et al., 2015; Ingle et al., 2010).

The Fe-isotope composition (δ^{56}Fe) of plume-influenced basalts from between 95.5°W and 85.5°W on the GSC varies from δ^{56}Fe $= +0.052\%$ to δ^{56}Fe $= +0.145\%$, with two outliers at δ^{56}Fe $= +0.216\%$ and δ^{56}Fe $= +0.242\%$. These two basalts with anomalously heavy δ^{56}Fe are from 90.95°W (TR164 26D-3g) and 86.3°W (ST7-17D-1g) and are distinguished by the fact that they possess the most enriched trace-element signatures (e.g. [La/Sm]$_n$) of any basalt measured along the GSC. In addition, the δ^{56}Fe composition of the remaining samples are typically heavier in regions of the GSC where radiogenic isotopes and trace-element ratios provide evidence for a greater contribution of enriched plume material (89.5°W–92.5°W; Gibson and Richards, 2018; Ingle et al., 2010), revealing a systematic relationship between the δ^{56}Fe composition of the GSC basalts and delivery of enriched plume material to the spreading ridge.

Our data reveals that D-MORBs and many N-MORBs from the GSC possess δ^{56}Fe signatures that lie at or below the lower end of those previously measured in MORBs (0.07‰ to $+0.14$‰; Teng et al., 2013). In addition, no clear difference is observed in the Fe-isotope composition of basalts from the eastern and western GSC (although the lowest values are observed in D-MORBs from the eastern GSC). This indicates that either: (i) there is no difference in the lithological properties/Fe-isotope composition of the depleted Eastern (DGM) and enriched WD plume components; or (ii) the relative fraction of Fe sourced from the WD component along the western GSC is small.

The δ^{56}Fe compositions measured in the GSC basalts show strong correlations with major element parameters (Na$_8$ and Ca$_8$/Al$_8$; fractionation corrected to 8 wt% MgO), and even stronger correlations with incompatible trace-element ratios indicative of both source enrichment and melting processes (e.g. [Ce/Yb]$_n$; [Sm/Yb]$_n$; Fig. 3). No obvious relationship between δ^{56}Fe and radiogenic isotope ratios (e.g. ^{206}Pb/^{204}Pb) are observed, which, can be explained by mixing relationships where the difference in the concentration of Pb (or Sr; Nd and Hf) in melts derived from the enriched and depleted mantle components are large (e.g. [Pb]$_{Enr}$/[Pb]$_{Dep}$ = 10–100; Fig. 3). Whilst melts of pyroxenite and/or eclogite components may possess FeO concentrations that are significantly different than melts of a peridotite (Lambart et al., 2013), these differences are unlikely to be as large as those predicted for incompatible trace-elements such as Pb or Sr. As a result, mixing curves between an enriched and depleted melt composition are highly curved, re-creating the observed values in the GSC basalts (Fig. 3d).

6. Discussion

The heterogeneity observed in the δ^{56}Fe composition of the GSC basalts may indicate that there is substantial variability in the lithological properties of the mantle source beneath the GSC. However, to constrain this further it is necessary to evaluate the influence that variations in mantle melting, crystallisation processes, and/or fO_2 may have on the δ^{56}Fe composition of the GSC basalts.

6.1. Fractional crystallisation

Several studies have investigated the influence of crystal fractionation on the δ^{56}Fe composition of basaltic magmas, but conflicting results indicate that the exact influence of magmatic differentiation is difficult to constrain and may vary between different tectonic settings (McCoy-West et al., 2018; Schuessler et al., 2009; Sossi et al., 2012; Teng et al., 2008). In general, it is assumed that isotopically-light Fe is fractionated into olivine and pyroxene (McCoy-West et al., 2018; Sossi et al., 2012; Teng et al., 2013). This fractionation is driven by the high Fe^{3+} content of basaltic melts compared to these mineral phases as several studies have shown that little to no fractionation of Fe-isotopes occur between olivine and highly reduced basalts that contain no Fe^{3+} (Dauphas et al., 2014; Prissel et al., 2018). In addition, the extent of Fe-isotope fractionation is highly dependent on whether: (i) the system is open or closed to oxygen exchange (Sossi et al., 2012); (ii) isotopic fractionation is controlled by equilibrium and/or kinetic processes (McCoy-West et al., 2018); and (iii) chromite fractionates alongside olivine and hence sequesters isotopically-heavy Fe from the melt phase (McCoy-West et al., 2018).

Table 1

Major-element, Fe-isotope and key trace-element ratio composition of the GSC basalts analysed in this study. Also shown is the magnitude of the fractional crystallisation correction applied to the Fe-isotope data.

| Sample	Latitude (°N)	Longitude (°W)	SiO_2	TiO_2	Al_2O_3	FeO_t	MnO	MgO	CaO	Na_2O	K_2O	P_2O_5	$\delta^{56}Fe$	2*s.d.	$\delta^{57}Fe$	2*s.d.	$\Delta^{56}Fe_{raw-corr}$	$[La/Sm]_n$	$[Sm/Yb]_n$
ST7 7D1g-1g	3.2	83.04	50.01	1.22	15.12	8.96	0.18	8.50	12.03	2.25	0.04	0.09	0.081	0.024	0.141	0.092	−0.007	0.45	0.95
DS D-2Ag	1.74	85.12	49.33	1.58	15.71	8.57	0.17	8.22	11.71	2.83	0.08	0.20	n/a	n/a	n/a	n/a	0.013	0.70	1.20
Ds D-1Ag	0.71	85.5	48.53	3.93	11.21	18.28	0.30	4.41	8.76	2.51	0.20	0.42	n/a	n/a	n/a	n/a	0.021	0.64	1.03
ST7 17D-1g	0.82	86.13	47.92	2.63	15.65	9.67	0.17	6.83	9.01	3.61	1.13	0.52	0.242	0.022	0.347	0.079	−0.004	2.42	2.30
CTW 6D-1g	0.85	86.55	49.87	2.12	12.96	12.96	0.24	6.47	10.34	2.44	0.11	0.18	0.053	0.026	0.082	0.010	0.029	0.68	1.02
CTW 7D1g-1g	0.86	87.09	50.35	1.00	14.96	8.91	0.17	8.46	12.51	2.11	0.02	0.07	0.063	0.031	0.076	0.036	0.012	0.42	0.88
TR164 1D-2g	0.74	87.48	49.61	2.29	12.38	14.36	0.26	5.68	9.96	2.70	0.14	0.19	0.086	0.008	0.132	0.016	0.017	0.74	1.04
TR164 3D-1g	0.73	88.24	50.02	1.57	13.72	11.60	0.23	7.25	11.30	2.29	0.10	0.14	0.089	0.015	0.140	0.034	0.006	0.71	0.99
TR164 5D-2g	0.78	88.9	49.71	1.68	13.64	11.43	0.22	6.98	11.41	2.57	0.13	0.16	0.086	0.039	0.121	0.061	0.023	0.75	1.15
CTW 9D-1g	0.78	89.23	49.38	1.61	14.11	10.76	0.20	7.40	11.87	2.57	0.14	0.13	0.101	0.024	0.139	0.044	0.022	0.93	1.10
TR164 6D-1g	0.84	89.59	49.41	2.29	14.15	10.57	0.17	6.07	10.42	3.07	0.67	0.35	0.145	0.005	0.227	0.041	0.002	1.93	1.72
TR164 6D-2g	0.84	89.59	49.48	2.27	14.27	10.66	0.20	6.11	10.48	3.08	0.69	0.34	0.141	0.024	0.203	0.020	0.016	1.98	1.64
TR164 9D-1g	0.93	90.5	47.72	2.03	15.96	9.85	0.16	7.56	11.32	2.95	0.37	0.22	0.115	0.012	0.167	0.014	0.031	1.43	1.76
TR164 27D-3g	1.06	90.81	49.12	1.98	14.09	10.99	0.22	6.89	11.53	2.78	0.26	0.19	0.094	0.006	0.124	0.055	0.013	1.17	1.43
TR164 26D-3g	1.9	90.95	49.57	2.69	14.89	9.80	0.16	5.59	9.79	3.12	1.13	0.48	0.216	0.024	0.303	0.054	0.022	2.41	2.05
TR164 25D-2g	1.95	91.18	50.21	1.75	13.40	12.01	0.23	6.64	10.97	2.52	0.16	0.15	0.102	0.015	0.133	0.010	0.015	1.44	1.40
TR164 24D-3g	1.96	91.24	49.55	2.08	13.46	12.27	0.23	6.42	10.82	2.64	0.27	0.19	0.091	0.013	0.132	0.029	0.015	1.16	1.06
CTW 10D-1g	1.99	91.61	50.40	1.56	13.52	11.57	0.23	6.92	11.40	2.53	0.21	0.13	0.088	0.017	0.125	0.046	0.001	1.09	1.21
TR164 11D-1g	2.09	92.24	49.18	2.05	14.17	11.21	0.21	6.57	11.24	3.02	0.32	0.23	0.134	0.031	0.215	0.062	0.019	1.30	1.37
TR164 12D-1g	2.25	92.69	50.13	1.42	14.20	10.78	0.21	7.51	12.02	2.47	0.17	0.14	0.076	0.018	0.139	0.029	−0.002	0.98	1.14
TR164 23D-2g	2.29	92.9	51.17	1.72	13.62	11.96	0.23	6.62	10.76	2.56	0.23	0.19	0.120	0.010	0.165	0.072	0.013	1.01	1.08
TR164 14D-1g	2.47	93.76	48.35	1.67	15.75	9.58	0.17	8.15	11.62	2.48	0.30	0.19	0.089	0.005	0.115	0.012	0.013	0.95	0.97
TR164 16D-1g	2.56	94.45	51.23	1.68	13.59	12.10	0.23	6.96	10.95	2.41	0.16	0.16	0.086	0.025	0.122	0.035	−0.009	0.86	1.03
TR164 17D-1g	2.57	94.87	49.97	1.79	13.35	12.46	0.21	6.95	10.62	2.48	0.19	0.19	0.080	0.020	0.128	0.004	−0.004	0.93	1.07
DS D-5g	2.44	95.62	49.54	1.17	15.53	9.02	0.17	8.69	11.91	2.28	0.08	0.10	0.103	0.023	0.148	0.041	−0.004	0.67	1.09
TR164 18D-3g	2.29	96.18	50.29	1.14	14.61	9.56	0.19	8.31	12.39	2.43	0.05	0.08	0.057	0.014	0.080	0.044	−0.004	0.43	1.05
TR164 19D-1g	2.12	97.19	49.73	1.24	14.93	9.30	0.19	8.28	12.05	2.30	0.05	0.09	0.051	0.024	0.077	0.042	−0.007	0.53	0.97
TR164 20D-1g	2.24	97.86	49.81	1.32	15.20	9.42	0.20	8.32	11.88	2.26	0.08	0.10	0.111	0.029	0.167	0.008	0.013	0.60	0.95
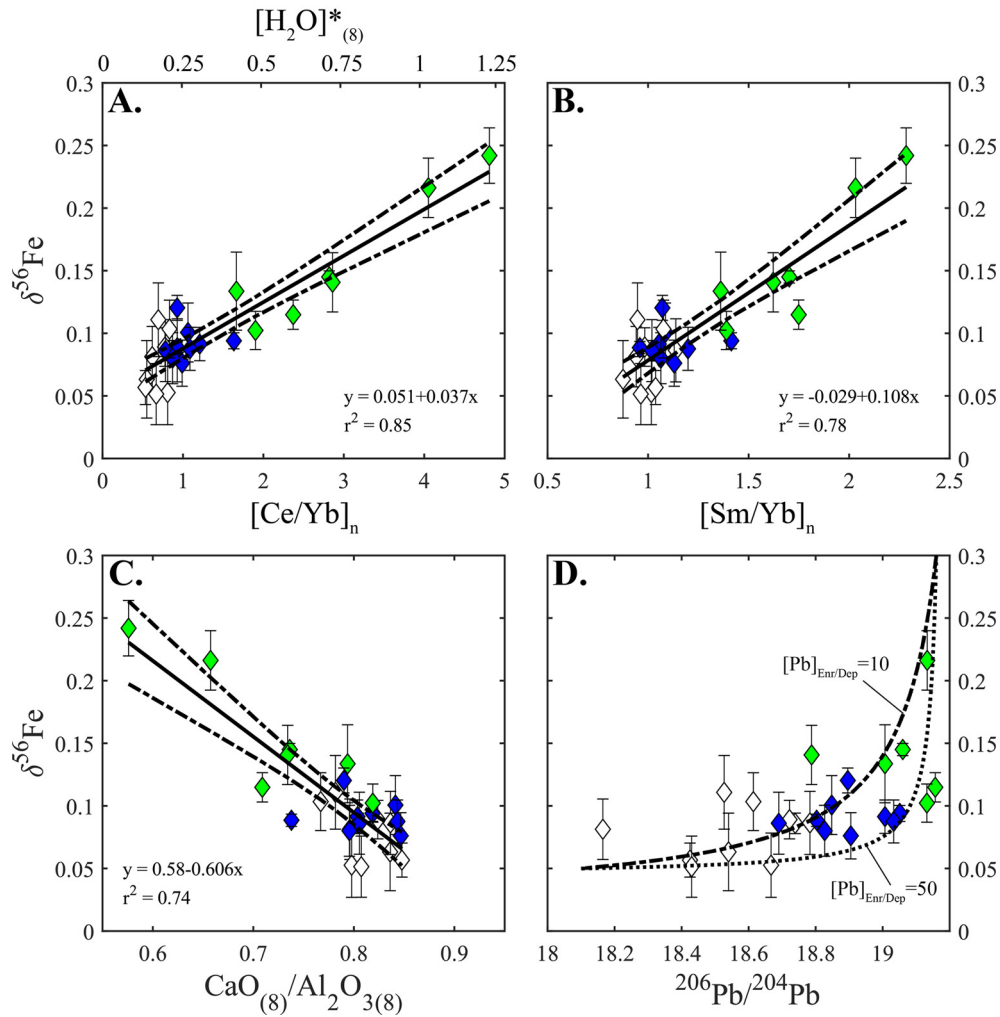
Fig. 3. Key correlations are observed between major- and trace-element parameters and the δ^{56}Fe composition of the GSC basalts. The strongest correlations are seen between δ^{56}Fe and REE ratios (**A.** and **B.**). We have used the $[Ce/Yb]_n$ composition of the GSC basalts to estimate their H_2O content at 8 wt% MgO (termed $[H_2O]^*_{(8)}$) following the method outlined in Gibson and Richards (2018). Panel **C.** shows the correlation between δ^{56}Fe and the fractionation corrected CaO/Al_2O_3 composition of the GSC basalts. This relationship may be indicative of a link between δ^{56}Fe and lithological heterogeneity in the sub-ridge mantle. Panel **D.** shows the relationship between δ^{56}Fe and $^{206}Pb/^{204}Pb$. Mixing curves between an enriched and depleted melt indicate that the lack of any significant correlation is expected. All plots shown display the measured δ^{56}Fe data (i.e. uncorrected for fractional crystallisation). It is, however, important to note that these correlations are unchanged by the fractional crystallisation correction applied in this study. In other words, these correlations do not represent artefacts of fractional crystallisation. (For interpretation of the colours in the figure, the reader is referred to the web version of this article.)

As the GSC basalts that we have analysed have a narrow range of MgO ($\sim$5.5–8.5 wt%), the influence of crystal fractionation on δ^{56}Fe is minimised and we have avoided any complications caused by the fractionation of isotopically-heavy magnetite in more evolved magmas (<5 wt% MgO; Sossi et al., 2012). Nevertheless, to ensure that our results are not influenced by variations in magmatic differentiation (E-MORBs tend to possess slightly lower MgO contents than D-MORBs) we have corrected the Fe-isotope, major- and trace-element composition of our samples to 8 wt% MgO using published mineral-melt trace-element partition coefficients and isotope fractionation factors (Sossi et al., 2016; full details can be found in Appendix A).

Due to the considerable uncertainties regarding the influence of crystallisation on the Fe-isotope composition of basaltic lavas, other fractionation factors between olivine/pyroxene and the melt phase were tested to ensure that our results are independent of our fractional crystallisation correction (e.g. from Dauphas et al., 2014; Appendix A). In addition, by applying a correction to 8 wt% MgO, within the range displayed by the GSC basalts, rather than Mg# $\sim$ 70 (i.e. in equilibrium with mantle peridotite), which

would require significant extrapolation, we minimise the propagated error that results from this correction.

Our fractionation-corrected dataset displays considerable δ^{56}Fe heterogeneity and confirms that magmatic differentiation does not have a major influence on the variation observed in the δ^{56}Fe composition of the GSC basalts. This demonstrates that significant heterogeneity in the composition of primary mantle melts beneath the GSC must exist. Below we consider whether this variability is related to melting processes (e.g. melt fraction, presence of garnet), or due to heterogeneity in the mantle source (oxidised/lithologically distinct components).

6.2. Melt fraction and fO$_2$

As outlined above, heavy Fe isotopes (i.e. ^{56}Fe and ^{57}Fe) are expected to be preferentially partitioned into Fe^{3+} bearing phases (e.g. basaltic melt). As a result, primary mantle melts should possess heavier δ^{56}Fe signatures than their source regions (Dauphas et al., 2014). In theory, this effect should be greatest for early-formed, low-fraction melts that (due to the incompatible nature of Fe^{3+}) are predicted to possess a higher proportion of Fe^{3+} than
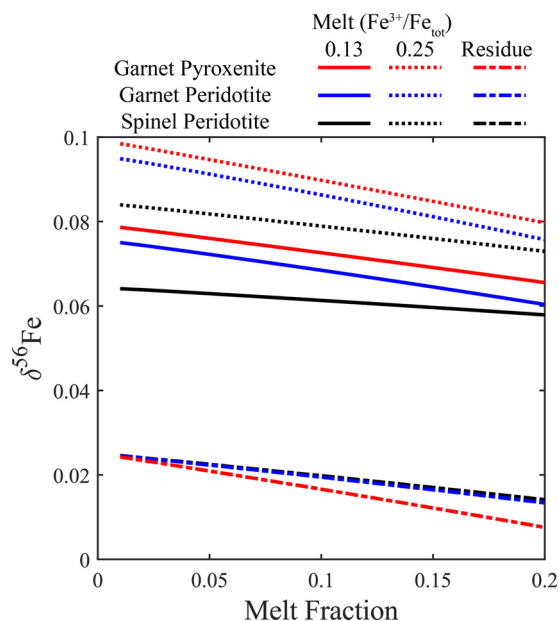
Fig. 4. Fe-isotope composition predicted during fractional melting of (i) garnet peridotite; (ii) spinel peridotite; and (iii) garnet pyroxenite. Melts of a garnet pyroxenite are predicted to be marginally heavier than those of a spinel peridotite, but this variation is not large enough to explain the heterogeneity in the composition of the GSC basalts. A larger difference is seen due to variations in the Fe^{3+}/Fe_{tot} ratio of the resulting melt, but this is still not large enough to explain the heterogeneity observed in the GSC basalts. For these calculations we take melting equations and FeO contents from Williams and Bizimis (2014) for spinel peridotites and garnet pyroxenites, and from Afonso et al. (2008) for garnet peridotites. (For interpretation of the colours in the figure, the reader is referred to the web version of this article.)

high-fraction melts (Dauphas et al., 2014, 2009). In addition, an increase in the fO_2 of the source (and therefore an increase in the Fe^{3+} available to enter the melt phase) is predicted to result in larger fractionation of Fe-isotopes during mantle melting (Dauphas et al., 2014, 2009).

However, there is no clear relationship between Fe^{3+}/Fe_{tot} and indices of melt fraction (e.g. Na_8) for the global MORB dataset (Cottrell and Kelley, 2011) and recent experimental work has shown that the Fe^{3+}/Fe_{tot} of peridotite partial melts remains approximately constant during partial melting (Sorbadere et al., 2018). Nevertheless, it is constructive to consider the maximum Fe-isotope composition that may be produced by low-fraction melting of a highly-oxidised source ($\sim$QFM+2), and whether or not these hypothetical melts may explain the composition of the GSC basalts.

To test this hypothesis, we present a new model to calculate the influence of fO_2 on the $\delta^{56}Fe$ composition of mantle melts. Our model uses published NRIXS (Nuclear Resonant Inelastic X-ray Scattering) measurements of melt Fe-O force constants in basaltic glass, to quantify the influence of Fe^{3+}/Fe_{tot} (Dauphas et al., 2014), alongside theoretical constraints on the Fe-O force constant for all Fe-bearing mantle minerals (Sossi and O'Neill, 2017) to calculate the $\delta^{56}Fe$ composition of melts formed during melting of mantle peridotite (see Appendix A for details). The results of this analysis indicate that the $\delta^{56}Fe$ composition of melts characterised by very high Fe^{3+}/Fe_{tot} ratios ($\sim$0.25) are only $\sim +0.02‰$ $\delta^{56}Fe$ heavier than the $\delta^{56}Fe$ composition of relatively reduced melts ($Fe^{3+}/Fe_{tot} = 0.13$; Fig. 4). Therefore, although the early model of Dauphas et al. (2009) indicates that highly oxidised melts may have a $\delta^{56}Fe$ composition as high as $\sim +0.18‰$ (Konter et al., 2016), we consider it unlikely that variations in fO_2 can explain the heterogeneity observed in the $\delta^{56}Fe$ composition of the GSC basalts.

In addition, none of the basalts from the GSC represent melts of the enriched mantle component alone. Therefore, the $\delta^{56}Fe$ com-

position of the enriched (and presumably oxidised) melt that is required to explain the GSC data is far heavier than that measured in the enriched GSC basalts. To constrain the $\delta^{56}Fe$ composition of melts from the enriched mantle component that would be required to explain the $\delta^{56}Fe$ heterogeneity of the GSC basalts we estimated the proportion of melt from the enriched mantle component which is needed to explain the incompatible trace-element composition of each basalt. This is done using: (i) a 2-component mantle melting model combined with; (ii) a Markov Chain Monte Carlo (MCMC) algorithm that evaluates and compares the melt composition predicted by each model and the measured REE composition of each GSC basalt (Fig. 5; see Appendix A for details). In all models shown in this study we assume that the primary control on the incompatible trace-element composition of the GSC basalts is the relative velocity of active upwelling below the anhydrous peridotite solidus, consistent with previous studies (e.g. Ingle et al., 2010; Appendix A).

The proportion of enriched melt generated in each model, as well as the proportion of melt that is derived from the garnet stability-field, is recorded alongside the deviation between the trace-element composition predicted by each model and the REE composition of each sample. These results are used to generate a probability distribution for the proportion of melt from the enriched mantle component that contributes to the formation of each sample along the GSC (Fig. 5; Appendix A) and reveal a strong correlation between $\delta^{56}Fe$ and the mass fraction contribution of enriched melt (Fig. 6a). Using this correlation, we can estimate the $\delta^{56}Fe$ composition of melts from the enriched mantle component that would be required to recreate the GSC data. This analysis is carried out for 3 separate scenarios, where melts of the enriched mantle component have FeO concentrations that are: (i) equivalent to ($\delta^{56}Fe = +0.445 \pm 0.050‰$); (ii) 1.5 times greater than ($\delta^{56}Fe = +0.355 \pm 0.038‰$); and (iii) 2 times greater than ($\delta^{56}Fe = +0.309 \pm 0.033‰$) the FeO concentration of melts from the depleted mantle component (Fig. 6a). The results clearly demonstrate that in all scenarios these end-member melt compositions cannot be recreated by any reasonable model of Fe-isotope fractionation during mantle melting of a peridotite mantle (e.g. Dauphas et al., 2009). Therefore, even though the moderately enriched basalts from the GSC have similar $\delta^{56}Fe$ compositions to that predicted by the model of Dauphas et al. (2009), variations in melt fraction and/or fO_2 cannot explain the $\delta^{56}Fe$ heterogeneity observed in the GSC basalts.

6.3. Influence of isotopically-light garnet

Data from both natural samples (Williams et al., 2009), and experimental studies (Sossi and O'Neill, 2017), have shown that garnet preferentially incorporates isotopically-light Fe-isotopes compared to other mantle minerals. It has therefore been hypothesised that primary mantle melts derived from the garnet-stability field may possess heavy Fe-isotope compositions compared to melts from the spinel-stability field (due to the retention of light Fe-isotopes in residual garnet; Nebel et al., 2018; Sossi and O'Neill, 2017). This is an attractive explanation for the heterogeneity observed in the GSC basalts, due to the very strong correlation observed between $\delta^{56}Fe$ and $[Sm/Yb]_n$ (Fig. 3), as well as the strong correlation between $\delta^{56}Fe$ and the proportion of melt derived from the garnet-stability field that is estimated by our MCMC models (Fig. 6b).

However, using theoretical constraints on the garnet-olivine fractionation factors (Sossi and O'Neill, 2017), and our new models of Fe-isotope fractionation during mantle melting, we show the heaviest $\delta^{56}Fe$ signature that results from small amounts of partial melting of a garnet lherzolite with $\delta^{56}Fe = +0.025‰$ is $\sim +0.075$ to $+0.095‰$, depending on the Fe^{3+}/Fe_{tot} content of the resulting
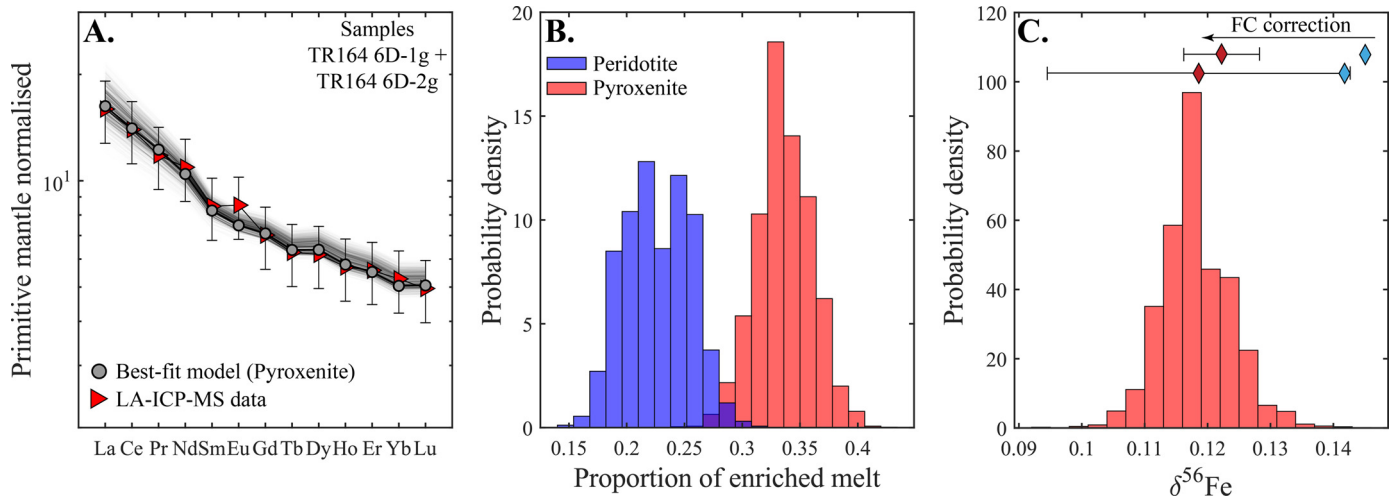
Fig. 5. Results of our mantle melting models. Panel **A.** shows the average trace-element composition of samples TR164 6D-1g and TR164 6D-2g (chosen as these represent E-MORBs with moderately elevated δ^{56}Fe signatures) and the trace-element composition of mantle melts predicted by our mantle melting models (grey lines). In this case all model compositions that are shown represent the compositions predicted by melting of a mantle that contains a pyroxenitic component and the grey circles represent the model that shows the closest match to the trace-element data of these two samples. Panel **B.** shows probability distributions for the proportion of enriched melt that is required to explain the composition of these samples when: (i) a 2-peridotite mantle is used (blue); and (ii) a peridotite-pyroxenite mantle is used (red). Panel **C.** shows the Fe-isotope composition predicted by melting a peridotite-pyroxenite mantle (see Methods for details of calculations). In this case the peridotite is assigned a δ^{56}Fe value of $+0.01$‰ (consistent with the highly depleted trace-element composition predicted for this component), and the pyroxenitic component is given a δ^{56}Fe composition of $+0.20$‰. The δ^{56}Fe composition predicted by our models provides an accurate match to the δ^{56}Fe composition measured in these two samples (red = fractionation corrected data; blue = raw data). (For interpretation of the colours in the figure, the reader is referred to the web version of this article.)

melt (Fig. 4). This estimate is significantly lighter than a significant number ($\sim$6–7) of the E-MORBs from the GSC, and much lighter than the extremely heavy δ^{56}Fe value of melts from the garnet stability-field that are required to match the data from the GSC (δ^{56}Fe = $+0.439 \pm 0.053$‰ for $[Fe]_{deep}/[Fe]_{shallow} = 1$, and δ^{56}Fe = $+0.304 \pm 0.036$‰ for $[Fe]_{deep}/[Fe]_{shallow} = 2$; Fig. 6b). As such, the correlation between δ^{56}Fe and $[Sm/Yb]_n$ does not indicate a causative link between the presence of garnet in a lherzolitic mantle residue and the δ^{56}Fe composition of the GSC basalts. Therefore, significant lithological heterogeneity and/or heterogeneity in the source δ^{56}Fe composition must exist to explain the large range observed in the Fe-isotope composition of the GSC basalts.

6.4. Fe-isotope heterogeneity of a metasomatised peridotite

Before we can consider the possibility that the δ^{56}Fe heterogeneity displayed by the GSC basalts is caused by variations in the contribution of melts from a pyroxenitic lithology, we need to evaluate whether these compositions could result from incorporation of melts from an isotopically heavy peridotite component. To do so, we take the heaviest δ^{56}Fe value measured in a metasomatized peridotite from Weyer and Ionov (2007; δ^{56}Fe = $+0.17$‰), and apply a source-melt fractionation of 0.05–0.08‰ (the largest isotopic fractionation predicted by our mantle melting models; Fig. 4). The results of our modelling indicate that the heaviest δ^{56}Fe value of a melt from a metasomatized peridotite is $\sim +0.22$–0.25‰, approximately equivalent to the heaviest value measured in any of the GSC basalts. It is important to note, however, that this value is still too low to recreate the range of δ^{56}Fe compositions observed in the GSC basalts unless it is assumed that sample ST7-17D-1g (from 86.13°W) represents a pure (un-mixed) melt of the enriched mantle component (Fig. 6a). This is considered highly unlikely as this sample has a relatively low MgO concentration (6.83 wt%) and is therefore likely to have undergone significant homogenisation in sub-ridge magma storage regions (Shorttle et al., 2016). Therefore, melting of an isotopically heavy, metasomatized peridotite cannot recreate the δ^{56}Fe composition of the GSC basalts.

6.5. Lithological heterogeneity

To investigate whether the Fe-isotope heterogeneity identified in the GSC basalts tracks lithological heterogeneity in the underlying mantle we use a simple 2-component mantle melting model (based on the Melt-PX model of Lambart et al., 2016) to simulate melting of a compositionally depleted peridotite and an enriched pyroxenite (Appendix A). The major-element composition of the pyroxenite component was set as the M5-40 composition from Lambart et al. (2013), a garnet websterite that lies close to the mean composition of the natural pyroxenite population (Appendix A). We model the trace-element composition of this component as a mixture between depleted peridotitic mantle and recycled crustal components (see Appendix A for details). Other proposed compositions for mantle pyroxenites were tested and the results indicate that the δ^{56}Fe composition of the pyroxenite-derived melt that is estimated below represents a maximum value (i.e. by using other pyroxenitic compositions less heterogeneity in the Fe-isotope composition of the mantle source is required to explain our results; Fig S.4).

Our Melt-PX based mantle melting model was coupled to a MCMC algorithm (as described above) in order to estimate the proportion of pyroxenite-derived melt that contributes to each GSC basalt (Fig. 5). Our results allow us to estimate the δ^{56}Fe of the pure pyroxenite melt, which is required to explain the heterogeneity observed in the GSC basalts, when the concentration of Fe is: (i) equivalent in melts derived from the two components (δ^{56}Fe = $+0.341 \pm 0.037$‰); and (ii) $\sim$1.5 times greater in melts derived from the pyroxenitic source component, which is reasonable given that melts of a pyroxenitic source often possess greater concentrations of FeO (Lambart et al., 2013) (δ^{56}Fe = $+0.281 \pm 0.031$‰; Fig. 6c). These estimates are remarkably similar to the heaviest δ^{56}Fe measured in any OIB globally (δ^{56}Fe = $+0.31$ to $+0.34$‰; Fig. 6c; Konter et al., 2016).

Our pyroxenite melting model also enables us to calculate the extent of Fe-isotope fractionation that is expected during melting of a peridotite-pyroxenite mantle (Fig. 5; Fig. 6). The δ^{56}Fe composition of the primary mantle melt formed at each pressure increment is calculated using theoretical and experimental
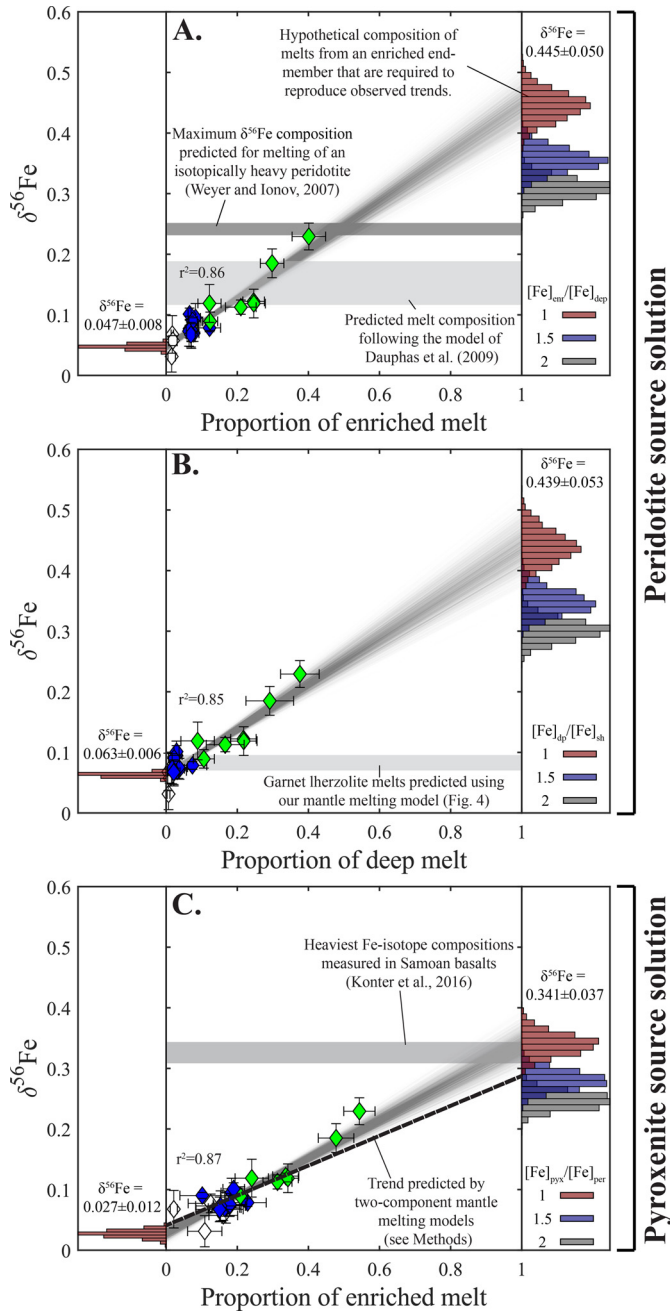
Fig. 6. The results of our Monte Carlo mantle melting models for a peridotite source (**A.** and **B.**) and pyroxenite source solution (**C.**) are shown. The composition of the end-member melts (shown by the histograms on each graph) were calculated by generating 1000 regression lines through the data where on every iteration each sample was positioned randomly according to their uncertainties. These results indicate that the $\delta^{56}Fe$ composition of enriched or deep melts (i.e. melts derived from the garnet-stability field) that are required to explain the $\delta^{56}Fe$ heterogeneity in the GSC basalts (assuming a peridotitic source) are far heavier than predicted by any reasonable model of mantle melting. This analysis was carried out for scenarios where the concentration of Fe in the enriched (or deep) melt is assumed to be: (i) equivalent to (red); (ii) 1.5 times greater than (blue); or (iii) 2 times greater than (grey) that in the depleted (or shallow) melt. (For interpretation of the colours in the figure, the reader is referred to the web version of this article.)

constraints on Fe-O force constants in basaltic melt and mantle minerals (Dauphas et al., 2014; Sossi and O'Neill, 2017). As expected, the modelled $\delta^{56}Fe$ composition of melts from the pyroxenitic source are heavier than those from the peridotite source, especially if the resulting melts are assumed to be slightly more oxidised than those of a depleted peridotite (Fig. 4). Nevertheless,

to generate the highest $\delta^{56}Fe$ compositions displayed by the GSC basalts we require the pyroxenitic source beneath the GSC to be isotopically-heavy ($\delta^{56}Fe = +0.18$ to $+0.20$‰; Fig. 5; Fig. 6). This estimate is remarkably similar to the predicted composition of pyroxenitic material that forms due to subduction and subsequent melting of isotopically heavy eclogite (Nebel et al., 2019), and is therefore considered as a reasonable estimate of the $\delta^{56}Fe$ composition of a mantle pyroxenite.

As a result, we suggest that the heterogeneity displayed by the GSC basalts is primarily driven by changes in the amount of pyroxenite-derived melt that is delivered to the sub-ridge magmatic sills/mush region. However, the presence of highly-enriched basalts, found only ~20 km away from 'moderately' enriched basalts, in regions of the GSC where there is no increase in crustal thickness (e.g. TR164 26D-3g; Mittelstaedt et al., 2014) cannot be explained by an anomalously large flux of melts from a pyroxenitic source to that segment of the GSC. Since the models above simply evaluate the relative proportion of pyroxenite- and peridotite-derived melt that contributes to each sample, these highly-enriched basalts may instead represent the incomplete mixing of high-pressure pyroxenite-derived melts with those sourced from an isotopically-depleted peridotite at shallower levels (Gibson and Richards, 2018; Rudge et al., 2013). Our results have important implications for plume-ridge interaction globally as they show that short length-scale heterogeneities in the geochemical composition of plume-influenced basalts may result from incorporation of melts from a plume-derived pyroxenitic lithology.

7. Implications

7.1. Lithological heterogeneity in the Galápagos mantle plume

Our new Fe-isotope data demonstrates that melts derived from a lithologically-distinct (i.e. pyroxenitic) component are present beneath the GSC. The relationship between lithological heterogeneity and heterogeneity in radiogenic isotope ratios in the Galapagos mantle plume is currently unclear (Vidito et al., 2013; Gleeson and Gibson, 2019). Here we attempt to constrain this uncertainty by establishing the radiogenic isotope composition of the enriched pyroxenitic plume component that is present beneath the GSC. We achieved this by iteratively adjusting the Sr, Nd and Pb isotope composition of the enriched pyroxenitic plume component in our Melt-PX based mantle melting models until the observed trace-element and radiogenic isotope composition of the eastern GSC basalts are reproduced (Fig. 7; chemical variations are related to variations in the relative upwelling velocity of the mantle). In this analysis, we attempt to re-produce the composition of the eastern GSC basalts as their radiogenic isotopic compositions result from mixing of melts from only two-components, avoiding any complications caused by the presence of the WD plume component beneath the western GSC. Our results indicate that the measured Sr, Nd and Pb isotope ratios of the GSC basalts cannot be reproduced by melting of a mantle source with extremely-radiogenic Pb-isotope signatures (i.e. FLO; Fig. 7). Instead, our analysis suggests that this component has a moderately radiogenic Pb-isotope signature ($^{206}Pb/^{204}Pb$ ~19.17). We note that our proposed Pb isotopic composition for the enriched pyroxenite source is similar to that of mildly alkaline basalts from western Santiago (Gibson et al., 2012). These basalts also possess high FeO and low CaO whole-rock contents that are characteristic of experimental melts of silica-undersaturated pyroxenite lithologies (e.g. M5-40; Lambart et al., 2013; Fig. S.3) and may suggest that a lithologically distinct (and previously unidentified) central component exists in the Galápagos mantle plume (Fig. 1; Fig. 7). More work is required to confirm this hypothesis, but it is supported by the absence of evidence for lithological heterogeneity in each of the 4
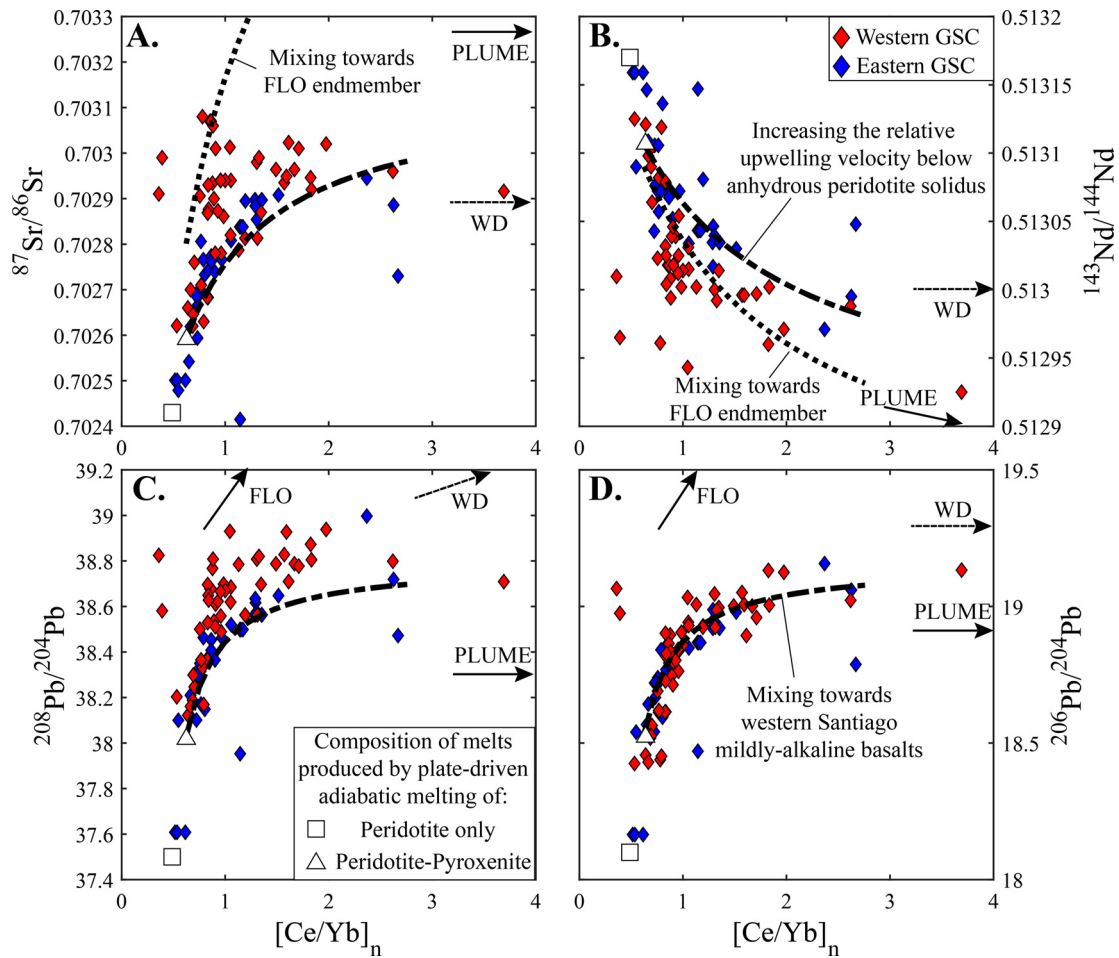
Fig. 7. Radiogenic isotope compositions of the GSC basalts plotted against trace-element enrichment $[Ce/Yb]_n$. The western GSC basalts are shown by red symbols and the eastern GSC symbols are shown by the blue symbols. The offset of the western and eastern GSC samples in Sr, Nd and Pb isotope space is due to the incorporation of a LREE-enriched component in the shallow mantle beneath the western GSC (WD component). Black lines show the radiogenic-isotope composition predicted by our mantle melting models as the rate of mantle upwelling below the anhydrous peridotite solidus is progressively increased. The dashed line represents a scenario where the enriched end-member has a moderately radiogenic Pb and Sr isotopic composition. In this scenario a very good match between the GSC data and the model predictions is observed ($^{206}Pb/^{204}Pb = 19.17$ and $^{208}Pb/^{204}Pb = 38.81$, equivalent to the most radiogenic Pb-isotope composition measured in any of the mildly alkaline basalts from Isla Santiago; Gibson et al., 2012). Our analysis also demonstrates that the FLO mantle component from Harpp and White (2001) does not contribute to the composition of the GSC basalts (dotted lines in panels **A.** and **B.**). Vectors displayed in all panels are directed towards where the radiogenic isotope composition of the Galápagos plume components intersect the right-hand y-axis ($[Ce/Yb]_n = 4$). (For interpretation of the colours in the figure, the reader is referred to the web version of this article.)

previously identified mantle components in the Galápagos mantle plume (Gleeson and Gibson, 2019; Vidito et al., 2013).

7.2. Global implications

The GSC basalts analysed in this study represent one of the first systematic studies of Fe-isotopes in a set of well-characterised oceanic basalts. Our new analyses reveal a large range in the $\delta^{56}Fe$ composition of the GSC basalts (+0.05 to +0.25‰), similar to a number of regions globally (e.g. Rochambeau Ridges in the Lau back-arc basin and Pitcairn; Fig. 8; Nebel et al., 2019, 2018). We have shown that this $\delta^{56}Fe$ heterogeneity is related to the lithological properties of the mantle source beneath the GSC (Fig. 9), which has important implications for our understanding of published Fe-isotope datasets of oceanic basalts (Konter et al., 2016; Nebel et al., 2013; Teng et al., 2013). For example, our results indicate that the highest $\delta^{56}Fe$ values measured in basalts from Samoa may result from melting of a pyroxenitic component with little to no involvement of peridotite-derived melts (Konter et al., 2016). Interestingly, the heavy $\delta^{56}Fe$ component that has been identified in the Samoan (and Pitcairn) lavas have distinctly different Pb-isotope signatures than that identified in the GSC basalts, indicating that the high $\delta^{56}Fe$ signature in oceanic

basalts is not related to the presence of a single mantle component (Konter et al., 2016; Nebel et al., 2019). In addition, the limited Fe-isotope data that exists for the Society Islands demonstrates that these basalts are notably heavier than most MORBs (Fig. 8; Weyer and Ionov, 2007). This may indicate the presence of a pyroxenitic component beneath these islands (as our models indicate that these moderately-heavy $\delta^{56}Fe$ compositions cannot be explained by lower melt extents or variations in fO_2), but more data is required to confirm this hypothesis. Similar observations can also be made for the Rochambeau Ridges in the Lau back-arc basin (Nebel et al., 2018).

Finally, a global compilation of MORB $\delta^{56}Fe$ compositions reveals a similar range to that observed in the GSC basalts (once the two most enriched samples are excluded; Nebel et al., 2013; Teng et al., 2013). The highest $\delta^{56}Fe$ values observed in MORBs ($\delta^{56}Fe \sim +0.17‰$) are found in EMORBs from the FAMOUS segment of the Mid-Atlantic Ridge (between 35°50′ to 37°20′N; Nebel et al., 2013), which are influenced by the Azores mantle plume. We suggest that the range in $\delta^{56}Fe$ compositions displayed by global MORBs may represent varying contribution from enriched, pyroxenitic components. However, more data is required to understand how this might relate to melts sourced from nearby mantle plumes. We propose that analysis of plume-influenced MORBs may
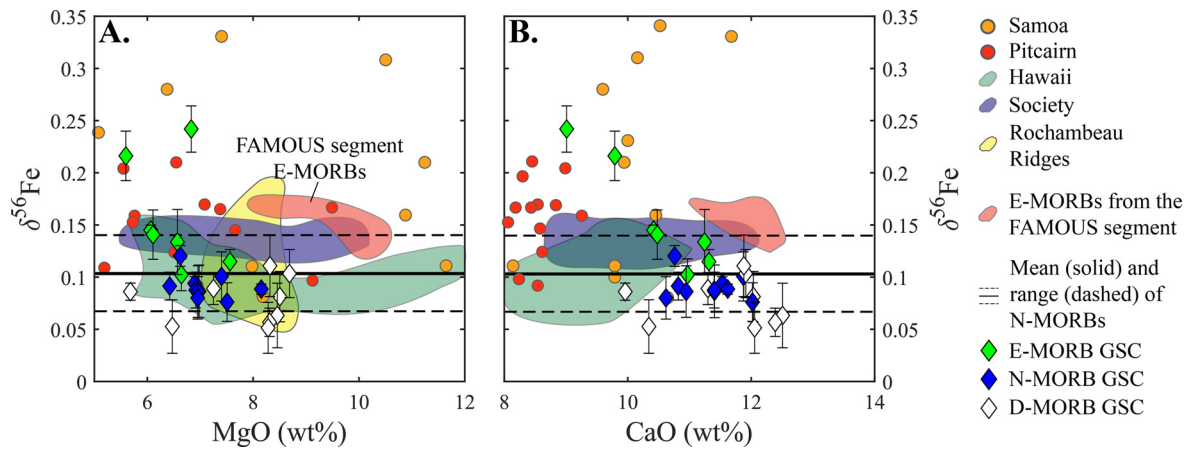
Fig. 8. Stable Fe-isotope variations in global oceanic basalts plotted against selected major-elements. It can be seen that the enriched MORBs from the FAMOUS segment plot at the upper end of the MORB field (Nebel et al., 2013; Teng et al., 2013), potentially indicating that these enriched samples may contain a significant contribution from a pyroxenitic source component. In addition, Fe-isotope compositions measured in basalts from various OIBs (e.g. Samoa and Pitcairn) have significantly elevated values that may indicate the presence of a pyroxenite component in the mantle source. Data from Konter et al. (2016); Nebel et al. (2019, 2018); Teng et al. (2013, 2008); Weyer and Ionov (2007). (For interpretation of the colours in the figure, the reader is referred to the web version of this article.)
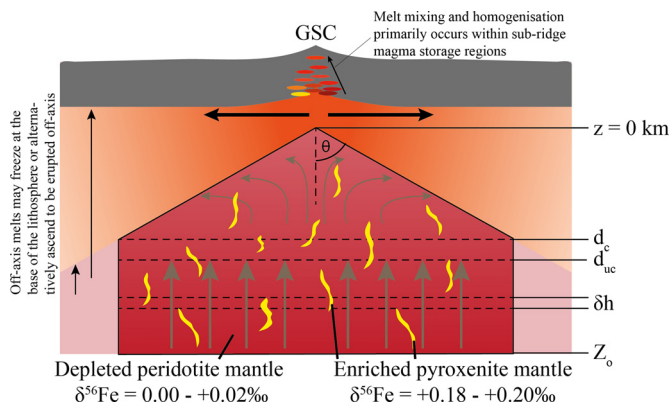

Fig. 9. Schematic illustration displaying the conceptual model by which the composition of melts from a 2-component mantle were calculated (see Appendix A for details). This shows a depth (d_c) below which the melting region (from which melts are extracted to be pooled at the ridge axis) is rectangular, a depth (d_{uc}) below which the relative upwelling velocity of the mantle is >1, and an incremental depth (δh) that represents the depth interval at which melt compositions were calculated in our model. This diagram also shows a key feature of our model, in that the sub-ridge mantle contains streaks and/or blebs of pyroxenitic material set in a peridotite matrix. Melt mixing and homogenisation is believed to occur in sub-ridge magma storage regions as recent studies have shown that the isotopic heterogeneity of melt entering the crust beneath oceanic spreading centres is very large (Lambart et al., 2019). (For interpretation of the colours in the figure, the reader is referred to the web version of this article.)

represent an effective way to constrain this relationship and identify the presence of pyroxenitic components in upwelling mantle plumes. Many plume-influenced ridges possess a number of very enriched basalts (as seen along the GSC) that represent an anomalously high contribution from melts of an isotopically-enriched mantle source (Gibson and Richards, 2018). Therefore, Fe-isotope analysis of these basalts may provide a unique insight into the extent of lithological heterogeneity in the convecting mantle.

8. Conclusions

The range of δ^{56}Fe compositions measured in the basalts from the Galápagos Spreading Centre ($+0.05$ to $+0.25$‰) is remarkably similar to that observed elsewhere (e.g. Lau basin; Nebel et al., 2018). New considerations of Fe-isotope fractionation during mantle melting, alongside Monte Carlo simulations of adiabatic decompression melting beneath an oceanic spreading centre, are used to show that the large variation observed in the δ^{56}Fe composition

of the GSC basalts cannot be related to melt fraction, the influence of isotopically-light garnet, or the fO_2 of a peridotitic source. However, we show that our new data is consistent with incorporation of melts from an isotopically-heavy pyroxenite source. In order to match the δ^{56}Fe composition of the GSC basalts our models indicate that this pyroxenitic component must have a source δ^{56}Fe composition of $\sim +0.18$ to $+0.20$‰, remarkably similar to the δ^{56}Fe composition of secondary pyroxenites predicted by Nebel et al. (2019). Our results therefore indicate that the heterogeneity observed in the δ^{56}Fe composition of the GSC basalts relates to variations in the proportion of pyroxenite-derived melt.

Our results have several key implications for our understanding of lithological heterogeneity in the Galápagos mantle plume as well as beneath MORBs and OIBs globally. Firstly, our results highlight that Fe-isotopes may provide an effective tracer of lithological heterogeneity in the Earth's convecting mantle. Secondly, our new Fe-isotope data confirms that a pyroxenitic component exists in the Galápagos mantle, possibly as short length scale heterogeneities beneath the central Galápagos. Finally, comparison of our new δ^{56}Fe data, and our new models of Fe-isotope fractionation during mantle melting, to the limited published datasets that exists for OIBs (e.g. Society) and enriched MORBs (e.g. FAMOUS on the Mid Atlantic Ridge) indicates that these basalts, with moderately-heavy δ^{56}Fe compositions, contain a significant contribution from melts of a isotopically-heavy pyroxenite.

Declaration of competing interest

The authors declare that they have no known competing financial interests or personal relationships that could have appeared to influence the work reported in this paper.

Acknowledgements

Appendix A. Supplementary material

Supplementary material related to this article can be found online at https://doi.org/10.1016/j.epsl.2020.116114.

References

Afonso, J.C., Fernàndez, M., Ranalli, G., Griffin, W.L., Connolly, J.A.D., 2008. Integrated geophysical-petrological modeling of the lithosphere and sublithospheric upper mantle: methodology and applications. Geochem. Geophys. Geosyst. 9. https://doi.org/10.1029/2007GC001834.

Christie, D.M., Werner, R., Hauff, F., Hoernle, K., Hanan, B.B., 2005. Morphological and geochemical variations along the eastern Galápagos Spreading Center. Geochem. Geophys. Geosyst. 6. https://doi.org/10.1029/2004GC000714.

Cottrell, E., Kelley, K.A., 2011. The oxidation state of Fe in MORB glasses and the oxygen fugacity of the upper mantle. Earth Planet. Sci. Lett. 305, 270–282. https://doi.org/10.1016/j.epsl.2011.03.014.

Craddock, P.R., Warren, J.M., Dauphas, N., 2013. Abyssal peridotites reveal the near-chondritic Fe isotopic composition of the Earth. Earth Planet. Sci. Lett. 365, 63–76. https://doi.org/10.1016/j.epsl.2013.01.011.

Cushman, B., Sinton, J., Ito, G., Eaby Dixon, J., 2004. Glass compositions, plume-ridge interaction, and hydrous melting along the Galápagos Spreading Center, 90.5°W to 98°W. Geochem. Geophys. Geosyst. 5. https://doi.org/10.1029/2004GC000709.

Dauphas, N., Craddock, P.R., Asimow, P.D., Bennett, V.C., Nutman, A.P., Ohnenstetter, D., 2009. Iron isotopes may reveal the redox conditions of mantle melting from Archean to Present. Earth Planet. Sci. Lett. 288, 255–267. https://doi.org/10.1016/j.epsl.2009.09.029.

Dauphas, N., Roskosz, M., Alp, E.E., Neuville, D.R., Hu, M.Y., Sio, C.K., Tissot, F.L.H., Zhao, J., Tissandier, L., Médard, E., Cordier, C., 2014. Magma redox and structural controls on iron isotope variations in Earth's mantle and crust. Earth Planet. Sci. Lett. 398, 127–140. https://doi.org/10.1016/j.epsl.2014.04.033.

Davis, F.A., Humayun, M., Hirschmann, M.M., Cooper, R.S., 2013. Experimentally determined mineral/melt partitioning of first-row transition elements (FRTE) during partial melting of peridotite at 3 GPa. Geochim. Cosmochim. Acta 104, 232–260. https://doi.org/10.1016/j.gca.2012.11.009.

Detrick, R.S., Sinton, J.M., Ito, G., Canales, J.P., Behn, M., Blacic, T., Cushman, B., Dixon, J.E., Graham, D.W., Mahoney, J.J., 2002. Correlated geophysical, geochemical, and volcanological manifestations of plume-ridge interaction along the Galápagos Spreading Center. Geochem. Geophys. Geosyst. 3, 1–14. https://doi.org/10.1029/2002GC000350.

Gale, A., Langmuir, C.H., Dalton, C.A., 2014. The global systematics of ocean ridge basalts and their origin. J. Petrol. 55, 1051–1082. https://doi.org/10.1093/petrology/egu017.

Gibson, S.A., Geist, D.G., Day, J.A., Dale, C.W., 2012. Short wavelength heterogeneity in the Galápagos plume: evidence from compositionally diverse basalts on Isla Santiago. Geochem. Geophys. Geosyst. 13. https://doi.org/10.1029/2012GC004244.

Gibson, S.A., Geist, D.J., Richards, M.A., 2015. Mantle plume capture, anchoring, and outflow during Galápagos plume-ridge interaction: mantle plume capture & outflow. Geochem. Geophys. Geosyst. 16, 1634–1655. https://doi.org/10.1002/2015GC005723.

Gibson, S.A., Richards, M.A., 2018. Delivery of deep-sourced, volatile-rich plume material to the global ridge system. Earth Planet. Sci. Lett. 499, 205–218. https://doi.org/10.1016/j.epsl.2018.07.028.

Gleeson, M.L.M., Gibson, S.A., 2019. Crustal controls on apparent mantle pyroxenite signals in ocean-island basalts. Geology 47 (4), 321–324. https://doi.org/10.1130/G45759.1.

Harpp, K.S., Geist, D.J., Koleszar, A.M., Christensen, B., Lyons, J., Sabga, M., Rollins, N., 2014. The geology and geochemistry of Isla Floreana, Galápagos: a different type of late-stage ocean island volcanism. In: Harpp, K.S., Mittelstaedt, E., d'Ozouville, N., Graham, D.W. (Eds.), Geophysical Monograph Series. John Wiley & Sons, Inc, Hoboken, New Jersey, pp. 71–117.

Harpp, K.S., White, W.M., 2001. Tracing a mantle plume: isotopic and trace element variations of Galápagos seamounts. Geochem. Geophys. Geosyst. 2. https://doi.org/10.1029/2000GC000137.

Hart, S.R., Hauri, E.H., Oschmann, L.A., Whitehead, J.A., 1992. Mantle plumes and entrainment: isotopic evidence. Science 256, 517–520. https://doi.org/10.1126/science.256.5056.517.

Herzberg, C., 2011. Identification of source lithology in the Hawaiian and Canary Islands: implications for origins. J. Petrol. 52, 113–146. https://doi.org/10.1093/petrology/egq075.

Hoernle, K., Werner, R., Morgan, J.P., Garbe-Schönberg, D., Bryce, J., Mrazek, J., 2000. Existence of complex spatial zonation in the Galápagos plume. Geology 28, 435. https://doi.org/10.1130/0091-7613(2000)28<435:EOCSZI>2.0.CO;2.

Hofmann, A.W., 1997. Mantle geochemistry: the message from oceanic volcanism. Nature 385, 219–229. https://doi.org/10.1038/385219a0.

Huang, F., Chakraborty, P., Lundstrom, C.C., Holmden, C., Glessner, J.J.G., Kieffer, S.W., Lesher, C.E., 2010. Isotope fractionation in silicate melts by thermal diffusion. Nature 464, 396–400. https://doi.org/10.1038/nature08840.

Ingle, S., Ito, G., Mahoney, J.J., Chazey, W., Sinton, J., Rotella, M., Christie, D.M., 2010. Mechanisms of geochemical and geophysical variations along the western Galápagos Spreading Center. Geochem. Geophys. Geosyst. 11. https://doi.org/10.1029/2009GC002694.

Konter, J.G., Pietruszka, A.J., Hanan, B.B., Finlayson, V.A., Craddock, P.R., Jackson, M.G., Dauphas, N., 2016. Unusual δ 56 Fe values in Samoan rejuvenated lavas generated in the mantle. Earth Planet. Sci. Lett. 450, 221–232. https://doi.org/10.1016/j.epsl.2016.06.029.

Kurz, M.D., Geist, D., 1999. Dynamics of the Galapagos hotspot from helium isotope geochemistry. Geochim. Cosmochim. Acta 63, 4139–4156. https://doi.org/10.1016/S0016-7037(99)00314-2.

Lambart, S., Baker, M.B., Stolper, E.M., 2016. The role of pyroxenite in basalt genesis: melt-PX, a melting parameterization for mantle pyroxenites between 0.9 and 5 GPa: melt-PX: pyroxenite melting model. J. Geophys. Res., Solid Earth 121, 5708–5735. https://doi.org/10.1002/2015JB012762.

Lambart, S., Koornneef, J.M., Millet, M.-A., Davies, G.R., Cook, M., Lissenberg, C.J., 2019. Highly heterogeneous depleted mantle recorded in the lower oceanic crust. Nat. Geosci. 12, 482–486. https://doi.org/10.1038/s41561-019-0368-9.

Lambart, S., Laporte, D., Schiano, P., 2013. Markers of the pyroxenite contribution in the major-element compositions of oceanic basalts: review of the experimental constraints. Lithos 160–161, 14–36. https://doi.org/10.1016/j.lithos.2012.11.018.

Lee, C.-T.A., Luffi, P., Plank, T., Dalton, H., Leeman, W.P., 2009. Constraints on the depths and temperatures of basaltic magma generation on Earth and other terrestrial planets using new thermobarometers for mafic magmas. Earth Planet. Sci. Lett. 279, 20–33. https://doi.org/10.1016/j.epsl.2008.12.020.

Matzen, A.K., Baker, M.B., Beckett, J.R., Wood, B.J., Stolper, E.M., 2017a. The effect of liquid composition on the partitioning of Ni between olivine and silicate melt. Contrib. Mineral. Petrol. 172. https://doi.org/10.1007/s00410-016-1319-8.

Matzen, A.K., Wood, B.J., Baker, M.B., Stolper, E.M., 2017b. The roles of pyroxenite and peridotite in the mantle sources of oceanic basalts. Nat. Geosci. 10, 530–535. https://doi.org/10.1038/ngeo2968.

McCoy-West, A.J., Fitton, J.G., Pons, M.-L., Inglis, E.C., Williams, H.M., 2018. The Fe and Zn isotope composition of deep mantle source regions: insights from Baffin Island picrites. Geochim. Cosmochim. Acta 238, 542–562. https://doi.org/10.1016/j.gca.2018.07.021.

Mittelstaedt, E., Soule, A.S., Harpp, K.S., Fornari, D., 2014. Variations in crustal thickness, plate rigidity, and volcanic processes throughout the Northern Galápagos Volcanic Province. In: Harpp, K.S., Mittelstaedt, E., d'Ozouville, N., Graham, D.W. (Eds.), Geophysical Monograph Series. John Wiley & Sons, Inc, Hoboken, New Jersey, pp. 263–284.

Nebel, O., Arculus, R.J., Sossi, P.A., Jenner, F.E., Whan, T.H.E., 2013. Iron isotopic evidence for convective resurfacing of recycled arc-front mantle beneath back-arc basins. Geophys. Res. Lett. 40, 5849–5853. https://doi.org/10.1002/2013GL057976.

Nebel, O., Sossi, P.A., Bénard, A., Arculus, R.J., Yaxley, G.M., Woodhead, J.D., Rhodri Davies, D., Ruttor, S., 2019. Reconciling petrological and isotopic mixing mechanisms in the Pitcairn mantle plume using stable Fe isotopes. Earth Planet. Sci. Lett. 521, 60–67. https://doi.org/10.1016/j.epsl.2019.05.037.

Nebel, O., Sossi, P.A., Foden, J., Bénard, A., Brandl, P.A., Stammeier, J.A., Lupton, J., Richter, M., Arculus, R.J., 2018. Iron isotope variability in ocean floor lavas and mantle sources in the Lau back-arc basin. Geochim. Cosmochim. Acta 241, 150–163. https://doi.org/10.1016/j.gca.2018.08.046.

Prissel, K.B., Krawczynski, M.J., Nie, N.X., Dauphas, N., Couvy, H., Hu, M.Y., Alp, E.E., Roskosz, M., 2018. Experimentally determined effects of olivine crystallization and melt titanium content on iron isotopic fractionation in planetary basalts. Geochim. Cosmochim. Acta 238, 580–598. https://doi.org/10.1016/j.gca.2018.07.028.

Putirka, K., Ryerson, F.J., Perfit, M., Ridley, W.I., 2011. Mineralogy and composition of the oceanic mantle. J. Petrol. 52, 279–313. https://doi.org/10.1093/petrology/egq080.

Rhodes, J.M., Huang, S., Frey, F.A., Pringle, M., Xu, G., 2012. Compositional diversity of Mauna Kea shield lavas recovered by the Hawaii Scientific Drilling Project: inferences on source lithology, magma supply, and the role of multiple volcanoes. Geochem. Geophys. Geosyst. 13. https://doi.org/10.1029/2011GC003812.

Rudge, J.F., Maclennan, J., Stracke, A., 2013. The geochemical consequences of mixing melts from a heterogeneous mantle. Geochim. Cosmochim. Acta 114, 112–143. https://doi.org/10.1016/j.gca.2013.03.042.

Schilling, J.-G., Fontignie, D., Blichert-Toft, J., Kingsley, R., Tomza, U., 2003. Pb-Hf-Nd-Sr isotope variations along the Galápagos Spreading Center (101°-83°W): Constraints on the dispersal of the Galápagos mantle plume. Geochem. Geophys. Geosyst. 4. https://doi.org/10.1029/2002GC000495.

Schuessler, J.A., Schoenberg, R., Sigmarsson, O., 2009. Iron and lithium isotope systematics of the Hekla volcano, Iceland – evidence for Fe isotope fractionation during magma differentiation. Chem. Geol. 258, 78–91. https://doi.org/10.1016/j.chemgeo.2008.06.021.

Shorttle, O., Maclennan, J., Lambart, S., 2014. Quantifying lithological variability in the mantle. Earth Planet. Sci. Lett. 395, 24–40. https://doi.org/10.1016/j.epsl.2014.03.040.

Shorttle, O., Rudge, J.F., Maclennan, J., Rubin, K.H., 2016. A statistical description of concurrent mixing and crystallization during MORB differentiation: implications

for trace element enrichment. J. Petrol. 57, 2127–2162. https://doi.org/10.1093/petrology/egw056.

Sobolev, A.V., Hofmann, A.W., Kuzmin, D.V., Yaxley, G.M., Arndt, N.T., Chung, S.-L., Danyushevsky, L.V., Elliott, T., Frey, F.A., Garcia, M.O., Gurenko, A.A., Kamenetsky, V.S., Kerr, A.C., Krivolutskaya, N.A., Matvienkov, V.V., Nikogosian, I.K., Rocholl, A., Sigurdsson, I.A., Sushchevskaya, N.M., Teklay, M., 2007. The amount of recycled crust in sources of mantle-derived melts. Science 316, 412–417.

Sorbadere, F., Laurenz, V., Frost, D.J., Wenz, M., Rosenthal, A., McCammon, C., Rivard, C., 2018. The behaviour of ferric iron during partial melting of peridotite. Geochim. Cosmochim. Acta 239, 235–254. https://doi.org/10.1016/j.gca.2018.07.019.

Sossi, P.A., Foden, J.D., Halverson, G.P., 2012. Redox-controlled iron isotope fractionation during magmatic differentiation: an example from the Red Hill intrusion, S. Tasmania. Contrib. Mineral. Petrol. 164, 757–772. https://doi.org/10.1007/s00410-012-0769-x.

Sossi, P.A., Nebel, O., Foden, J., 2016. Iron isotope systematics in planetary reservoirs. Earth Planet. Sci. Lett. 452, 295–308. https://doi.org/10.1016/j.epsl.2016.07.032.

Sossi, P.A., O'Neill, H.St.C., 2017. The effect of bonding environment on iron isotope fractionation between minerals at high temperature. Geochim. Cosmochim. Acta 196, 121–143. https://doi.org/10.1016/j.gca.2016.09.017.

Sun, S.-s., McDonough, W.F., 1989. Chemical and isotopic systematics of oceanic basalts: implications for mantle composition and processes. Geol. Soc. (Lond.) Spec. Publ. 42, 313–345. https://doi.org/10.1144/GSL.SP.1989.042.01.19.

Teng, F.-Z., Dauphas, N., Helz, R.T., 2008. Iron isotope fractionation during magmatic differentiation in Kilauea Iki Lava Lake. Science 320, 1620–1622. https://doi.org/10.1126/science.1157166.

Teng, F.-Z., Dauphas, N., Helz, R.T., Gao, S., Huang, S., 2011. Diffusion-driven magnesium and iron isotope fractionation in Hawaiian olivine. Earth Planet. Sci. Lett. 308, 317–324. https://doi.org/10.1016/j.epsl.2011.06.003.

Teng, F.-Z., Dauphas, N., Huang, S., Marty, B., 2013. Iron isotopic systematics of oceanic basalts. Geochim. Cosmochim. Acta 107, 12–26. https://doi.org/10.1016/j.gca.2012.12.027.

van der Hilst, R.D., Widiyantoro, S., Engdahl, E.R., 1997. Evidence for deep mantle circulation from global tomography. Nature 386, 578–584. https://doi.org/10.1038/386578a0.

Vidito, C., Herzberg, C., Gazel, E., Geist, D., Harpp, K., 2013. Lithological structure of the Galápagos Plume: lithological structure Galpagos Plume. Geochem. Geophys. Geosyst. 14, 4214–4240. https://doi.org/10.1002/ggge.20270.

Villagómez, D.R., Toomey, D.R., Geist, D.J., Hooft, E.E.E., Solomon, S.C., 2014. Mantle flow and multistage melting beneath the Galápagos hotspot revealed by seismic imaging. Nat. Geosci. 7, 151–156. https://doi.org/10.1038/ngeo2062.

Weyer, S., Ionov, D.A., 2007. Partial melting and melt percolation in the mantle: the message from Fe isotopes. Earth Planet. Sci. Lett. 259, 119–133. https://doi.org/10.1016/j.epsl.2007.04.033.

White, W.M., McBirney, A.R., Duncan, R.A., 1993. Petrology and geochemistry of the Galápagos Islands: portrait of a pathological mantle plume. J. Geophys. Res., Solid Earth 98, 19533–19563. https://doi.org/10.1029/93JB02018.

Williams, H.M., Bizimis, M., 2014. Iron isotope tracing of mantle heterogeneity within the source regions of oceanic basalts. Earth Planet. Sci. Lett. 404, 396–407. https://doi.org/10.1016/j.epsl.2014.07.033.

Williams, H.M., Nielsen, S.G., Renac, C., Griffin, W.L., O'Reilly, S.Y., McCammon, C.A., Pearson, N., Viljoen, F., Alt, J.C., Halliday, A.N., 2009. Fractionation of oxygen and iron isotopes by partial melting processes: implications for the interpretation of stable isotope signatures in mafic rocks. Earth Planet. Sci. Lett. 283, 156–166. https://doi.org/10.1016/j.epsl.2009.04.011.

Yaxley, G.M., Green, D.H., 1998. Reactions between eclogite and peridotite: mantle refertilisation by subduction of oceanic crust. Schweiz. Mineral. Petrogr. Mitt. 78, 243–255.

Zhao, X., Zhang, Z., Huang, S., Liu, Y., Li, X., Zhang, H., 2017. Coupled extremely light Ca and Fe isotopes in peridotites. Geochim. Cosmochim. Acta 208, 368–380. https://doi.org/10.1016/j.gca.2017.03.024.